

The rotor as a sensor — Observing shear and veer from the operational data of a large wind turbine

Marta Bertelè^{1,2}, Paul J. Meyer³, Carlo R. Sucameli¹, Johannes Fricke³, Anna Wegner³, Julia Gottschall³, and Carlo L. Bottasso¹

¹Wind Energy Institute, Technische Universität München, Boltzmannstr. 15, 85748 Garching bei München, Germany

²Siemens Gamesa Renewable Energy, Beim Strohhause 17-31, 20097 Hamburg, Germany

³Fraunhofer Institute for Wind Energy Systems IWES, Am Seedeich 45, 27572 Bremerhaven, Germany

Correspondence: C. L. Bottasso (carlo.bottasso@tum.de)

Abstract.

This paper demonstrates the observation of wind shear and veer directly from the operational response of a wind turbine equipped with blade load sensors. Two independent neural-based observers, one for shear and one for veer, are first trained using a machine learning approach, and then used to produce estimates of these two wind characteristics from measured blade load harmonics. The study is based on a data set collected at an experimental test site, featuring a highly-instrumented 8 MW wind turbine, an IEC-compliant met mast, and a vertical profiling lidar reaching above the rotor top.

The present study reports the first demonstration of the measurement of wind veer with this technology, and the first validation of shear and veer with respect to lidar measurements spanning the whole rotor height. Results are presented in terms of correlations, exemplary time histories and aggregated statistical metrics. Measurements of shear and veer produced by the observers are very similar to the ones obtained with the widely adopted profiling lidar, while avoiding its complexity and associated costs.

1 Introduction

The goal of this paper is to demonstrate the observation of wind shear and veer, directly from the operational response of a wind turbine. This is achieved by the concept of the rotor as a sensor where the blades, scanning the flow field, are used to measure relevant characteristics of the inflow. A key advantage of this approach, termed *wind sensing*, is that it does not require extra hardware, but simply relies on the standard operational data available in the supervisory control and data acquisition (SCADA) system, in addition to blade load measurements. Although the latter are not always available on all production turbines, they are becoming more and more widespread, as they are used for other functions, such as load mitigation and condition monitoring.

A novelty of this paper is the first ever – to the authors’ knowledge – demonstration of the observation of veer using this technology. This is made possible by the formulation recently proposed in Kim et al. (2023), where feed-forward neural networks are trained to estimate various wind characteristics from blade load harmonics. This machine-learning approach improves on various previous formulations based on the use of load harmonics, starting with the study of Bottasso and Riboldi (2014) and then further developed over the years, as more completely described in Bertelè et al. (2021) and references therein. In

addition to vertical shear and veer, load harmonics can be used to estimate horizontal shear and directions (lateral misalignment and upflow). However, load harmonics are not the only way to estimate wind inflow characteristics. For example, Bottasso et al. (2018) use the rotor blades as local scanning wind sensors, which produce estimates of the vertical and horizontal shears, the latter serving also as a wake detector (Schreiber et al., 2020).

A second novelty of the paper is the demonstration of the observation of shear (and veer) over the entire rotor disk. Although the field validation of shear has been reported before, previous studies were based on measurements from met masts reaching only up to hub height (Bertelè et al., 2021; Schreiber et al., 2020), and not to the top of the rotor. The present work is based on the BHV test site (Meyer and Gottschall, 2022), which features the large 8 MW AD8-180 wind turbine. In the framework of unrelated projects, the turbine was equipped with various sensors that include optical strain gauges along the blades (Wegner et al., 2022). The site is complemented by an IEC-compliant met mast and by a vertical-profiling pulsed scanning lidar, capable of reaching well above the rotor top.

Results reported in this paper indicate that both shear and veer can be measured by wind sensing, in general exhibiting a very good match with the corresponding measurements provided by the vertical profiling (VP) lidar, an IEC-approved and widely-adopted device for resource assessment and power performance testing (IEC, 2022). This is remarkable, because – when load sensors are already installed on a turbine – the measurement of these inflow quantities comes at no additional hardware purchase or maintenance cost, as the technology simply amounts to an on-board software upgrade.

Most turbines today operate based only on a very limited knowledge of the ambient conditions, as provided by the on-board anemometry system. Although this is the current standard, it is reasonable to expect that a more complete knowledge of the inflow might improve the way future turbines will be operated. As an example, the control of wakes might benefit from an improved knowledge of the inflow (Meyers et al., 2022). In fact, various studies have investigated and clarified the effects on wake path and recovery caused by shear (Fleming et al., 2014; Vollmer et al., 2016; Gebraad et al., 2016; Bromm et al., 2017) and veer (Vollmer et al., 2016). When the effects of shear and veer on wakes are of a similar order of magnitude as the ones caused by the control action (e.g., an intentional yaw misalignment), neglecting their presence will lead to a loss of performance. The shear and veer observers demonstrated here could inform a park controller of the inflow conditions at the rotor disk of each turbine in a farm (in contrast to a met mast, which will never be exactly co-located with a turbine, and only rarely will be exactly in front of it), at essentially no cost and with no extra hardware (in contrast with lidar-based solutions).

The paper is organized in two main parts. First, Sect. 2 presents the methods. Section 2.1 reviews the formulation of the shear and veer observers, following the approach developed by Kim et al. (2023). Next, Sect. 2.2 describes the BHV test site and its instrumentation. Finally, Sect. 2.3 describes the calculation of shear and veer from the lidar and mast measurements. This first methodological section is followed by Sect. 3, which presents the results. First, Sect. 3.1 discusses the training of the neural-based observers on a portion of the data set. Next, Sect. 3.2 provides an analysis of their performance on an independent validation data set, considering correlations between estimates and lidar-provided references, an exemplary time history, as well as aggregated statistical quality metrics. Finally, Sect. 4 concludes the work discussing its main findings.

2 Methods

2.1 Formulation of the shear and veer observers

Following Kim et al. (2023), the wind observer is formulated as

$$60 \quad y_E = \text{NN}(\mathbf{p}, \mathbf{x}_M), \quad (1)$$

where y represents a scalar wind characteristic, $\text{NN}(\cdot, \cdot)$ is a single-output neural network (Bishop, 2006) with free parameters \mathbf{p} , \mathbf{x} is the vector of N_x network inputs, while $(\cdot)_E$ and $(\cdot)_M$ respectively indicate estimated and measured quantities. In this work, two separate networks are considered, one for vertical linear wind shear κ_v , and one for vertical linear wind veer $\Delta\theta^1$.

Considering a single-hidden-layer feed-forward neural network with M hidden neurons, function $\text{NN}(\cdot, \cdot)$ writes

$$65 \quad \text{NN}(\mathbf{p}, \mathbf{x}) = \mathbf{w}^T \boldsymbol{\sigma}(\mathbf{V}^T \mathbf{x} + \mathbf{a}) + b, \quad (2)$$

where $\boldsymbol{\sigma}(\cdot)$ is a vector of sigmoid activation functions, V_{ij} and a_i are the synaptic weights and biases connecting the input layer with the hidden layer, whereas w_i and b connect the hidden layer with the output scalar y , with $i = [1, M]$ and $j = [1, N_x]$. These free model parameters are stored in vector $\mathbf{p} = \{\dots, w_j, \dots, V_{ij}, \dots, a_i, \dots, b\}^T$.

The free network parameters \mathbf{p} are trained by backpropagation to minimize the error cost function

$$70 \quad E(\mathbf{p}) = \frac{1}{N} \sum_{l=1}^N (y_{E_l}(\mathbf{p}, \mathbf{x}_{M_l}) - y_{M_l})^2 + W \frac{1}{N_p} \sum_{m=1}^{N_p} p_m^2, \quad (3)$$

where $N_p = M(N_x + 2) + 1$. The first term of the objective function drives the estimates y_{E_l} produced by the network towards the N available measurements y_{M_l} . The second term of the objective is a Bayesian regularization, which reduces the chances of being trapped in local minima (Burden and Winkler, 2009). The tunable coefficient W sets the relative weight of the Bayesian and error terms. The unknown network weights are iteratively corrected as $\Delta\mathbf{p} = -\eta \partial E(\mathbf{p}) / \partial \mathbf{p}$, where η is the learning rate.

75 The implementation of the neural network and its training is based on the Matlab Deep Learning Toolbox (Matlab, 2023).

The network input vector is defined as

$$\mathbf{x} = \{\mathbf{m}^T, V, \rho\}^T, \quad (4)$$

where \mathbf{m} is a vector of blade load harmonics, V is wind speed, and ρ is air density. The presence of wind speed V among the inputs accounts for the different behavior, control and deformation of the wind turbine in different operating conditions.

80 This scheduling wind speed is computed as a 30 sec moving average of the estimated rotor-effective wind speed (Soltani et al., 2013). The dependency on air density ρ accounts for the aerodynamic origin of the loads; further details are available in Kim et al. (2023).

¹As shown in Kim et al. (2023), a similar formulation can be used to estimate the horizontal shear as well as the yaw misalignment angle, although these quantities are not considered further in the present work. In fact, horizontal shear is presumably very modest at the test turbine of this study, since it is never waked by other machines. Additionally, only modest variations in yaw misalignment were observed during the present field trials, and therefore the data set does not contain significant-enough information to allow for the identification of a misalignment observer.

Harmonics are computed for the out- and in-plane load components, respectively noted $(\cdot)^{OP}$ and $(\cdot)^{IP}$, from the corresponding strain gauge signals via the Coleman-Feingold transformation (Coleman and Feingold, 1958), and then filtered to
 85 remove any remaining spurious noise. Following the analysis developed in Kim et al. (2023), only once-per-revolution (1P) harmonics are used for the vertical linear shear case, and vector \mathbf{m} is defined as

$$\mathbf{m} = \{m_{1c}^{OP}, m_{1s}^{OP}, m_{1c}^{IP}, m_{1s}^{IP}\}^T. \quad (5)$$

On the other hand, the estimation of linear veer requires a richer input including also the twice-per-revolution (2P) harmonics, leading to the following definition of vector \mathbf{m} :

$$90 \quad \mathbf{m} = \{m_{1c}^{OP}, m_{1s}^{OP}, m_{1c}^{IP}, m_{1s}^{IP}, m_{2c}^{OP}, m_{2s}^{OP}, m_{2c}^{IP}, m_{2s}^{IP}\}^T. \quad (6)$$

In the previous expressions, subscripts $(\cdot)_{ks}$ and $(\cdot)_{kc}$ respectively indicate kP sine and cosine harmonic amplitudes. A simple explanation of the harmonic content of the shear and veer observers is offered in Appendix A. Kim et al. (2023) offers a more detailed analysis of the relationship between inflow characteristics and harmonic content of the loads. The analysis developed there can be used to estimate the number of harmonics that are theoretically necessary in order to resolve a desired polynomial
 95 order in the shear and veer.

Both the simple analysis of the appendix and the more refined one of Kim et al. (2023) indicate that veer can be estimated based only on 2P harmonics. However, it was verified that an implementation based on both the 1P and 2P harmonics provides slightly more precise estimates; the results shown later are therefore based on the 1-2P implementation. The reason for this apparent discrepancy might be due to the approximate nature of the theoretical analysis, which is based on a number of
 100 simplifying assumptions.

Limiting the observer to the 1 and 2P harmonics has potential advantages over more complex implementations. First, higher harmonics are associated with higher-order variations of the inflow characteristics, which may be affected by the fast and small eddies in the flow caused by turbulence. Conversely, slower-varying inflow characteristics are mostly driven by changes in the stability of the atmosphere, which in turn drives wake path and recovery. If the goal of the observer is to inform a wind farm
 105 controller, these latter slower effects are of interest, whereas the former fast disturbances should be rejected (Meyers et al., 2022). Additionally, it is reasonable to assume that the lower harmonics between two turbines of the same type implementing the same controller will be similar, whereas higher harmonics might exhibit some increased turbine-to-turbine variability. Therefore, limiting the use to the sole 1 and 2P harmonics might make it possible to train the observers on a machine and then use it on another (of the exact same type), although there is not yet any direct proof of this assertion.

110 A graphical depiction of the neural observers for shear and veer is reported in Figs. 1a and 1b, respectively.

2.2 Test site

The shear and veer observers were identified and validated using wind field and turbine load measurements from the BHV test site (Meyer and Gottschall, 2022), a former airport located in close proximity to Bremerhaven, in the northwest of Germany next to the Weser river. The test site is built around the 8 MW research wind turbine AD8-180. Flat and homogeneous terrain

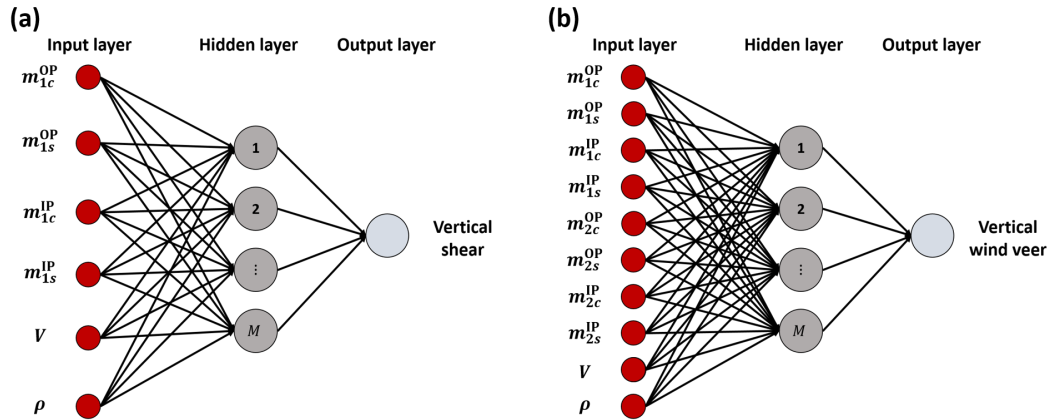


Figure 1. Graphical representation of the neural observer of vertical wind shear **(a)** and vertical wind veer **(b)**, with their respective inputs.

115 conditions are present in the westerly direction, whereas an urban terrain prevails in the easterly direction. Various wind and turbine-related measurements have already been carried out at this site, as reported in previously published studies (Giyanani et al., 2022; Huhn and Gómez-Mejía, 2022; Meyer and Gottschall, 2022; Hung et al., 2022; Wegner et al., 2022). The test site is shown in Fig. 2, with a view looking east.



Figure 2. View from west to east of the BHV test site, with the AD8-180 wind turbine on the left, and the met mast and VP lidar on the right.

The AD8-180, an 8 MW machine with a 180 m rotor diameter (D) and a 115 m hub height, is equipped with several sensors, including strain gauges placed at various spanwise positions along the blades. Operational data from the SCADA system, together with the strain gauge measurements, are available at a 25 Hz frequency. Flapwise and edgewise measurements from the strain gauges placed at blade root were converted into out and in-plane components, based on blade pitch angle. Next, using the azimuthal rotor position, the load signals were converted into 1 and 2P harmonics, to be used as network inputs (see Eq. 4).

An IEC-compliant met mast is installed at a distance of 399.3 m ($\approx 2.2D$) from the turbine, in the 189° direction. The mast is equipped with cup anemometers at five heights up to 114.7 m, as well as wind vanes at three heights reaching up to 110 m, i.e. just below the hub. Data from the mast is available at a sampling rate of 1 Hz. Additionally, a barometer, thermometer, and hygrometer are available to derive air density.

A VP lidar of the type WindCube V2 is installed next to the met mast, measuring wind speed and direction at heights from 40 m up to 290 m. Various studies have shown a good agreement between cup anemometers and VP lidars for the measurement of wind speed and direction (Gottschall et al., 2012; Clifton et al., 2018). Furthermore, the VP lidar is an established measurement device for power performance testing and wind resource assessment according to IEC 61400-50-2:2022 (IEC, 2022). The lidar sequentially measures line-of-sight velocities for a fixed scan pattern of 4 beams along a cone with half-opening angle of 28° , combined with one vertically scanning beam. Wind speed and direction are then reconstructed at each measured height from the line-of-sight velocities with every updated line-of-sight measurement, i.e. every 0.8 seconds. As the met mast provides wind speed and direction measurements only for the lower half of the rotor, the VP lidar is used for measuring these quantities from a height of 40 m to the top of the rotor.

A sketch of the relevant heights and distances of turbine, met mast and lidar are shown in Fig. 3. This study is based on a data set of synchronized turbine, mast and lidar measurements collected for 115 days within the period from 30 July to 12 December 2021. The data set contains significant variability of the ambient conditions as well as a large occurrence of southerly winds, where the met mast is directly upwind of the turbine.

2.3 Field measurements of shear and veer

The wind observer networks are trained based on measurements of the wind shear and veer, together with their corresponding network inputs, as expressed in the first term of the objective function given by Eq. (3).

In this work, wind shear and veer measurements were provided by the VP lidar. In fact, the VP lidar measures at 12 heights from 40 to 290 m above ground, thus including most of the rotor-swept area, which ranges from the lower blade tip (LBT) point $z_{\text{LBT}} = 25$ m to the higher blade tip (HBT) point $z_{\text{HBT}} = 205$ m.

Both for shear and veer, a linear best fit was first computed using the nine VP lidar measurements of wind speed V and direction Γ included within the rotor-swept area, i.e. between 40 and 195 m above ground (see Fig. 3). Next, shear and veer were computed as

$$\kappa_v = \frac{V(z_{\text{HBT}}) - V(z_{\text{LBT}})}{z_{\text{HBT}} - z_{\text{LBT}}}, \quad (7a)$$

$$\Delta\theta = \frac{\Gamma(z_{\text{HBT}}) - \Gamma(z_{\text{LBT}})}{z_{\text{HBT}} - z_{\text{LBT}}}, \quad (7b)$$

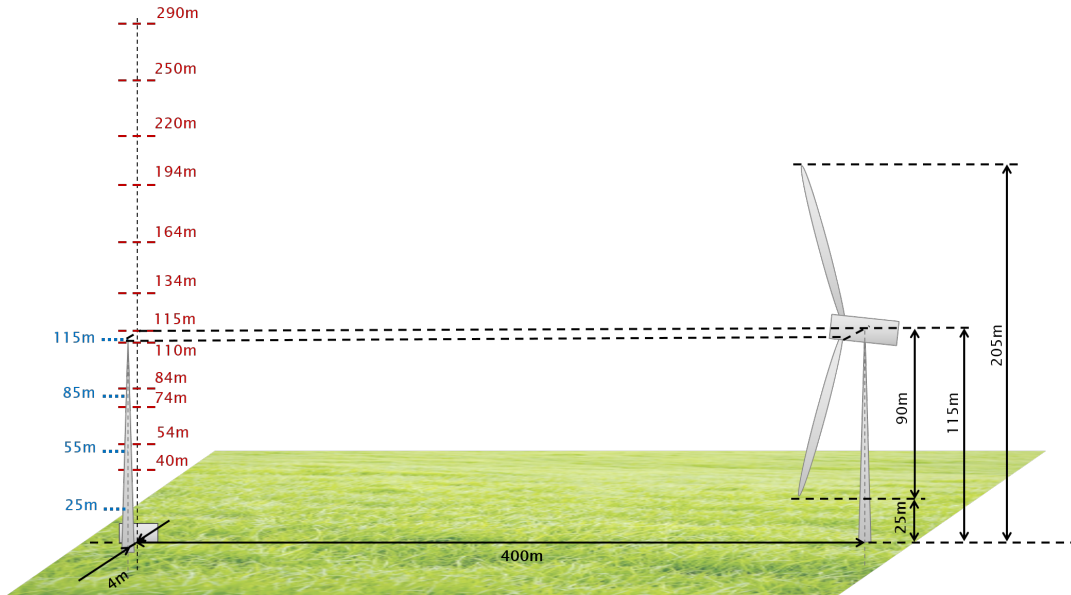


Figure 3. Sketch (to scale) of the test site with the relevant dimensions rounded to the next integer. Heights are given relative to ground level at the turbine location. Blue labels: met mast measurement heights; red labels: lidar measurement heights.

where the terms at the numerators of these two expressions are computed via the linear fit evaluated at the lower and higher blade tip points, respectively.

Before using these lidar-based rotor-effective wind characteristics for training, their accuracy was verified against the IEC-compliant met mast present at the site. Vertical shear and veer were derived from the mast measurements following the same linear-fitting procedure previously described for the lidar, i.e. using

$$\kappa_{v\text{Low}} = \frac{V(z_{\text{HUB}}) - V(z_{\text{LBT}})}{z_{\text{HUB}} - z_{\text{LBT}}}, \quad (8a)$$

$$\Delta\theta_{\text{Low}} = \frac{\Gamma(z_{\text{HUB}}) - \Gamma(z_{\text{LBT}})}{z_{\text{HUB}} - z_{\text{LBT}}}. \quad (8b)$$

Notice that, since the mast reaches only up to hub height z_{HUB} , the resulting shear and veer are defined over only the lower half of the rotor disk.

To perform a valid comparison, also the shear and veer derived from the lidar were computed over the lower part of the rotor, which was obtained by considering only measurements in the range from 40 to 115 m. Figure 4 shows the results of this comparison in the form of 10-min averages, reporting the met mast measurements on the x axis and the corresponding lidar quantities on the y axis. Wind speeds at hub height, shown in Fig. 4a, have a high Pearson coefficient R of 0.99 and a mean absolute error (MAE) of about 0.122 ms^{-1} . There is a high correlation also for wind shear and veer, which have Pearson coefficients of 0.97 and 0.95, respectively, as shown in Fig. 4b and c. In addition to the different measurement technology, differences might be caused by the fact that the mast reaches down to 25 m above the terrain, whereas the lowest measurement

point for the lidar is at 40 m. Figure 4c suggests the existence of a slight slope difference for veer. This might be caused by the met mast, because vertical veer is obtained only from two heights above ground, and possibly because of some minor misalignment of its wind direction sensors. Given its uncertain origin, lidar measurements were not recalibrated to eliminate this effect.

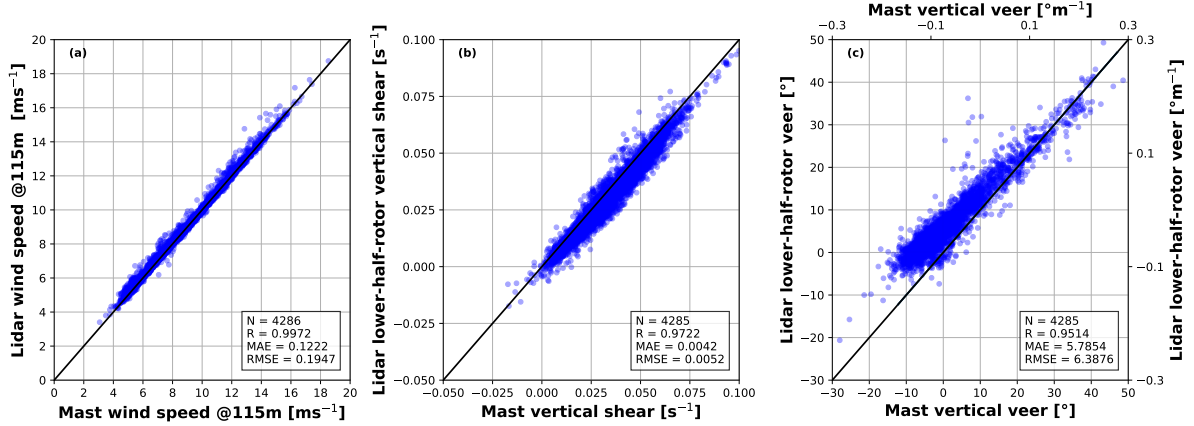


Figure 4. Correlation of 10-min averages of measured quantities from the met mast (x axis) and VP lidar (y axis). Hub-height wind speed (a); lower-half-rotor vertical shear (b); lower-half-rotor veer, both in absolute $[\circ]$ (i.e. between z_{LBT} and z_{HUB}) and in relative $[\circ m^{-1}]$ terms (c). Black solid line: ideal match; R: Pearson’s correlation coefficient; N: number of data points; MAE: mean absolute error; RMSE: root mean square error.

3 Results

The wind observers for shear and veer formulated in Sect. 2.1 were tested on a dataset collected at the site described in Sect. 2.2. The next pages explain first in Sect. 3.1 the identification of the observers from a subset of the data. Next, Sect. 3.2 presents the results obtained by using the observers on an independent validation subset.

3.1 Observer identification

The data set was cleaned, to retain only data points when the turbine was operational and all necessary measurements (SCADA, strain gauges, lidar) were available. This resulted in about 18 full days of valid data points, spread between August and December. The training subset was obtained by picking at random 67% of the data points (i.e. about 290 hours) within the whole set, to exclude effects due to seasonal variability. The remaining set (i.e. about 138 hours) was used for validation. Although in principle the observer could be trained directly on high-frequency data, following the example of Kim et al. (2023) 10-min averages were preferred, in order to mitigate the effects of possible outliers. The ranges and number of occurrences of values of wind speed V , air density ρ , vertical shear κ_v , and veer $\Delta\theta$ in the two data sets are shown in Fig. 5.

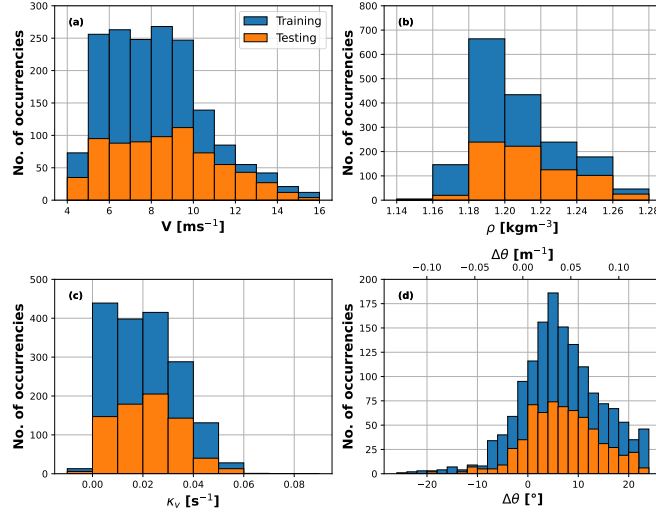


Figure 5. Range and number of occurrences of 10-min averages of wind speed (a), density (b), vertical shear (c), and wind veer (d). Blue: training data set; red: validation data set.

Air density ρ and wind speed V appearing in the network inputs (see Eq. 4) were measured as follows. Air density was derived from the available measurements of pressure, temperature, and humidity, using the ideal gas laws. Wind speed was obtained by means of an observer based on the standard SCADA signals of power, rotor speed and blade pitch (Soltani et al., 2013). The use of an observer, which is based only on standard operational data, renders the shear and veer observers usable on common production machines, where a lidar or a neighboring met mast might not be available. A MoWiT model (Fricke et al., 2021) of the AD8 turbine was used to generate offline a look-up table (LUT), storing the dependency of produced power on ambient wind speed, pitch angle and rotor speed, considering mechanical losses in the drive-train and the efficiency of the generator. Next, the LUT was inverted by a Newton iteration using the aerodynamic torque obtained from the dynamic torque-balance equation, and on measured power, pitch and rotor speed from the SCADA data stream; rotor acceleration was obtained by deriving with respect to time the measured rotor speed. Figure 6 shows the correlation between 10-min averages of the rotor-effective wind speed (REWS) from the observer, reported on the y axis, and the wind speed obtained by averaging the available lidar measurements along the rotor height, reported on the x axis. The match between these two quantities is characterized by a Pearson coefficient of 0.98 and a MAE of about 0.35 ms^{-1} .

Both for the shear and veer observers, the best-performing network configuration was found by trial and error to comprise of one single hidden layer and 10 neurons. Both networks took of the order of a few seconds for training on a standard desktop computer.

200 3.2 Shear and veer observer performance

After training, the two observers of shear and veer were tested on the 10 Hz 138-hour-long validation data set.

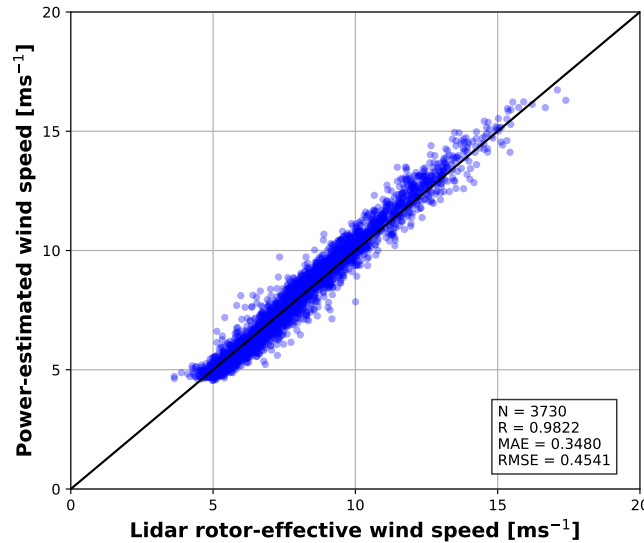


Figure 6. Correlation of 10-min averages between the rotor-average wind speed measured by the lidar (x axis) and the rotor-effective wind speed measured by the observer (y axis). Black dashed line: ideal match.

Figure 7 reports the results in terms of 10-min averages. Quantities estimated by the observers are reported on the y axis, while the lidar-measured references are on the x axis. Figure 7a indicates an excellent match for shear, with a Pearson coefficient $R = 0.947$ and an RMSE of about $4.015 \cdot 10^{-3} \text{ s}^{-1}$. Figure 7b indicates a slightly lower quality of the results for veer, with $R = 0.879$ and a larger scatter, as quantified by an RMSE of about 5.78° . MAEs are $3 \cdot 10^{-3} \text{ s}^{-1}$ and 4° , respectively, for shear and veer.

Exemplary time histories of observed and reference quantities are given in Fig. 8. Figure 8a and b show the estimated (red) and reference (blue) wind shear and veer, respectively. Additionally, Fig. 8c reports the wind direction at the site, where a horizontal black solid line indicates the 189° direction for which lidar and turbine are aligned. The observation of shear and veer was performed at 1 Hz, and results were then averaged with a 1 min moving window. The figures indicate that the observed quantities follow quite well their respective references, both in terms of trends and mean values. There is a particularly good match between 5 AM and 7 AM, when lidar and turbine are aligned, although some of the worst match is between 4 AM and 5 AM, when the two are also almost aligned. However, the two observes are clearly capable of detecting the diurnal cycle, characterized by a higher shear and veer during the night, but also rapid events such as the spike observed around 9:30 AM.

Finally, to provide with more statistically relevant results, Fig. 9a and b respectively show the MAEs of the observed shear and veer as functions of wind speed, for different turbulence intensity (TI) values. Figure 9c reports the number of available data hours for each specific speed and TI bin. MAEs were computed after averaging 1 Hz observations over 10 minutes, and then comparing them with their respective lidar-measured references. It is difficult to draw strong conclusions, as not all wind speed bins are equally populated. In the intermediate wind speed region – where more data points are available – it appears

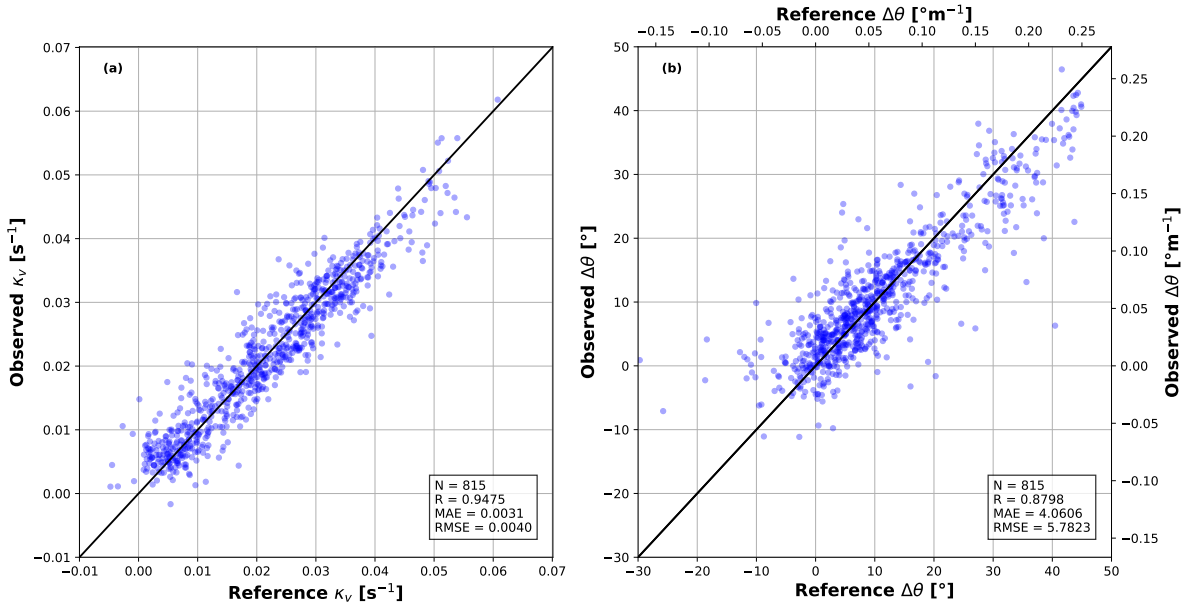


Figure 7. Correlation of 10-min averages between estimated wind characteristics (y axis) and their reference lidar-measured quantities (x axis). Vertical shear κ_v (a); wind veer $\Delta\theta$ (b). Black dashed line: ideal match.

220 that, as expected, errors are slightly larger for higher TI values. However, in the 7 to 11 ms^{-1} range there are more than twice the data points for low (5-10%) TI than for intermediate (5-10%) TI values. It also appears that errors might be increasing around the lowest and highest wind speeds. This could be due to the smaller loading on the wind turbine in these conditions, because of the small dynamic pressure at low wind speeds and of the large blade pitch at the higher ones. However, these findings should be confirmed by larger and better populated data sets.

225 4 Conclusions

This paper has demonstrated that it is possible to observe vertical wind veer from the operational response of a large wind turbine. The paper also performed the first validation of the observation of shear and veer over the full rotor height with respect to reference measurements obtained with a VP lidar. The study was conducted at the BHV test site using the highly instrumented 8 MW AD8-180 wind turbine. Additionally, the presence on site of an IEC-compliant met mast allowed for a
 230 comparison – although limited only to the lower half of the rotor – of the lidar-measured wind speed, shear and veer, enhancing the confidence in the results.

Based on the results reported herein, the following conclusions can be drawn:

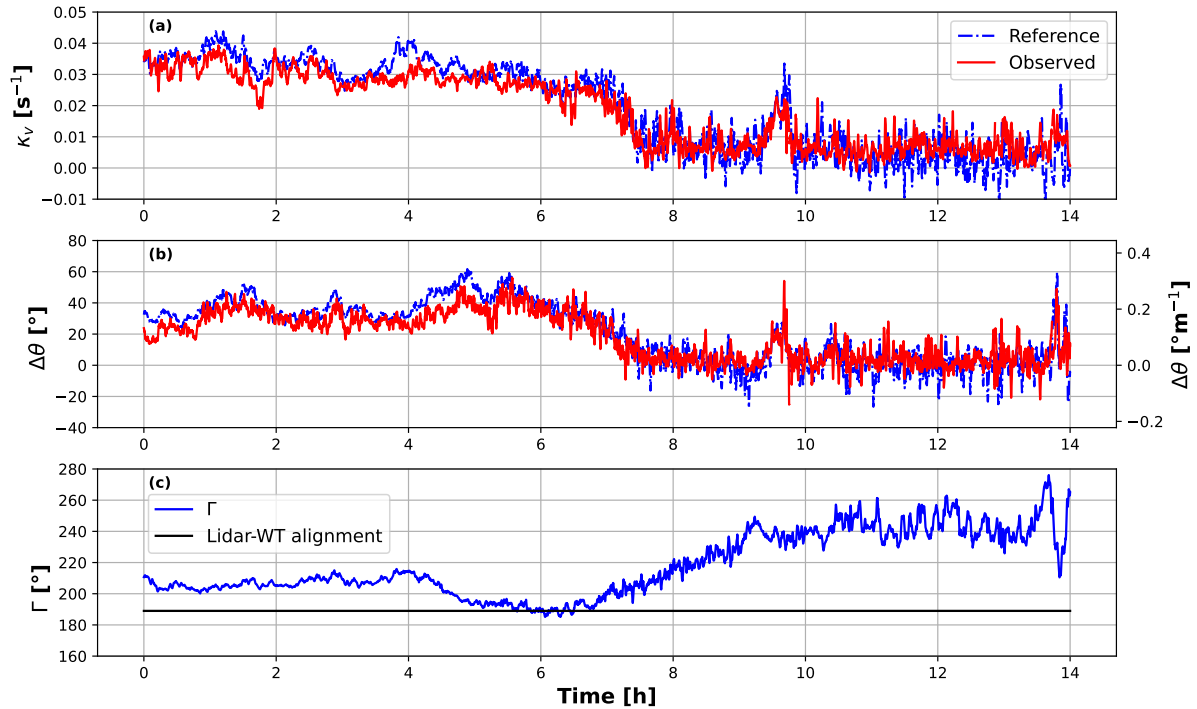


Figure 8. Time histories of vertical shear (a), wind veer (b), and wind direction measured at the mast (c). Blue: observed quantities; red: lidar-measured reference.

- The correlation between 10-min averages of the observed and lidar-measured shear and veer results in Pearson coefficients of $R = 0.947$ and $R = 0.879$, respectively. The quality of shear is presumably better because its observation relies only on 1P harmonics, whereas veer requires also the 2P components, which are probably more affected by turbulence.
- For the same reason, veer has a higher scatter than shear, as seen in Fig. 7.
- Both the shear and veer observers seem capable of tracking both slow and relatively fast changes in ambient conditions. In particular, the exemplary time history reported in Fig. 8 indicates the ability to follow changes of the duration of the order of tens of minutes with good accuracy. The examination of other similar time histories, not reported here for brevity, supports and confirms this finding.
- Definitive indications on the effects of TI and speed on the quality of the estimates are not possible because of the uneven population of the bins. However, results aggregated over the whole validation data set indicate typical MAEs in the neighborhood of 4° for veer and around $3 \cdot 10^{-3} \text{ s}^{-1}$ for shear.

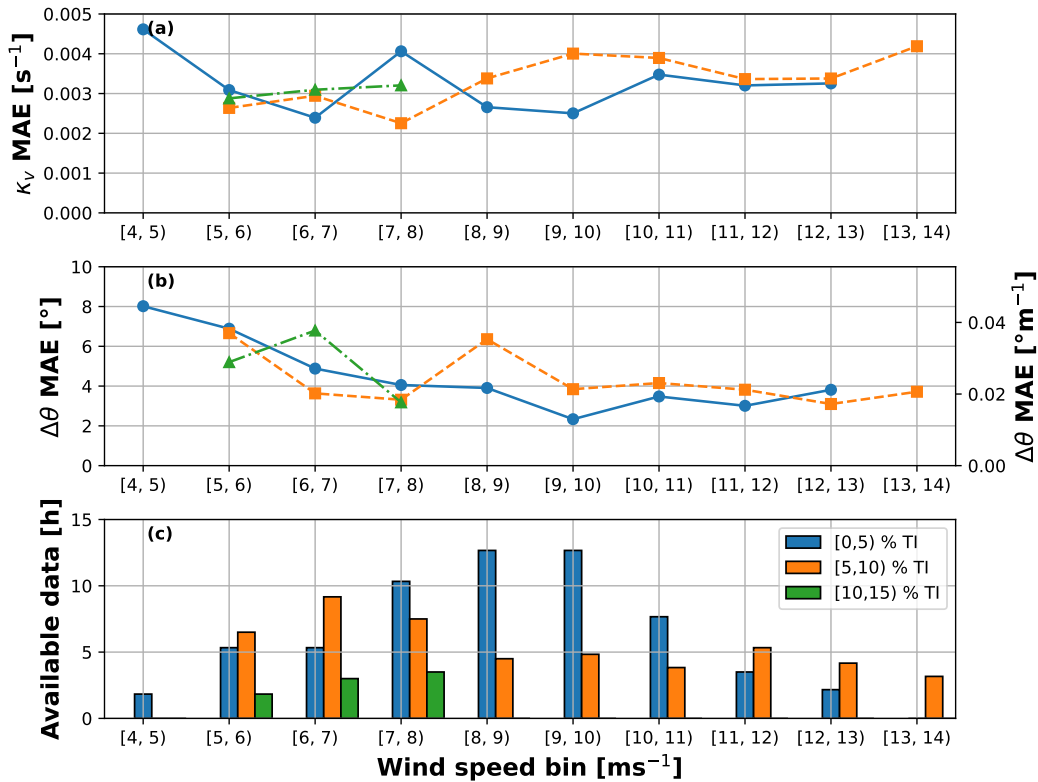


Figure 9. MAE of vertical shear κ_v (a) and wind veer $\Delta\theta$ (b), and hours of available data (c) vs. binned rotor-effective wind speed V , for different TI levels.

In general, these results seem to indicate the ability of the harmonic-based observers to estimate shear and veer from the operational response of a wind turbine, with a close match to the widely adopted vertical profiling lidar. In evaluating these results, however, two remarks are in order:

- The lidar measurements cannot be assumed as an absolute ground truth. In fact, as all measurements, they are affected by various sources of error, and they represent spatial and temporal averages that differ from the ones performed by the observer and by the anemometry installed on the mast. Additionally, the lidar is not exactly co-located with the turbine, it is not always exactly in front of it, and it does not even span exactly the same height, as it starts measuring a small distance above the LBT. Therefore, an exact match between observers and lidars cannot and should not, in general, be expected. One source of discrepancy could be removed by the use of a forward staring lidar, which would at least always provide wind measurements directly upwind of the turbine.

255 – Some of the speed and TI bins are not well populated, which might have some effect on the significance of the performance statistics. This source of uncertainty could be removed by the use of longer data sets, which however were not available for this study.

Appendix A: Harmonic content of the observers

Following Eggleston and Stoddard (1987), an elementary model of blade dynamics can be obtained by considering a rigid flapping blade, connected to the rigid hub by a hinge, as shown in Fig. A1.

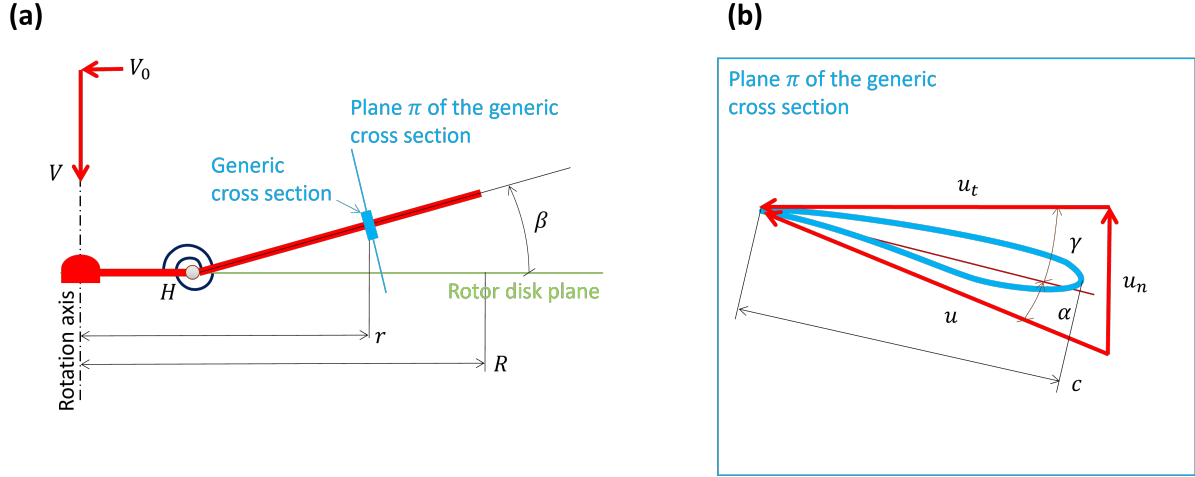


Figure A1. Elementary model of a flapping blade. **(a):** side view, with rigid flapping segment hinged at the rigid hub at point H . **(b):** view perpendicular to the plane of the cross section, showing the section-relative flow components u_n and u_t .

260 The flow speed components normal (noted u_n) and tangential (noted u_t) to a generic cross section of the flapping blade can be written

$$u_n = V(1 - a) - V\kappa_s \frac{r}{R} \cos \psi - V_0 \beta \sin \psi, \quad (\text{A1a})$$

$$u_t = \Omega r, \quad (\text{A1b})$$

where a is the axial induction, β is the (small) blade flap angle, ψ is the azimuthal blade position (where $\psi = 0$ when the blade is vertical pointing downwards), r is the spanwise position of the cross section, R the rotor radius, V_0 is the cross-flow (i.e., a lateral wind speed component parallel to the rotor disk plane), and Ω the rotor speed. When the inflow presents a veer $\Delta\theta$, the cross-flow can be written as $V_0 = \Delta\theta(r/R) \cos \psi$. The flapwise bending moment on the blade is obtained by integrating the lift L along the blade span, where

$$L = \frac{1}{2} \rho u^2 c C_{L_\alpha} \alpha \approx \frac{1}{2} \rho c C_{L_\alpha} (u_n u_t - \gamma u_t^2), \quad (\text{A2})$$

270 where $u \approx u_t$ is the flow speed at the blade section, c is the chord, $C_{L\alpha}$ is the lift slope, $\alpha \approx u_n/u_t - \gamma$ the angle of attack (considering small angles), and finally γ is the pitch angle.

Inserting the expression for u_n and u_t given by Eqs. (A1) into Eq. (A2), it follows that lift, and hence bending moments, depends on terms proportional to $\kappa_s \cos \psi$ and $\Delta\theta \sin \psi \cos \psi = 2\Delta\theta \sin(2\psi)$. Hence, shear leaves a mark on the 1P harmonic of blade loads, and veer on their 2P harmonics.

275 *Data availability.* Data from the field measurements can be requested to JG. All figures and the data used to generate them can be retrieved in Pickle Python and MATLAB formats via <https://doi.org/10.5281/zenodo.8335021> (Bertelè et al., 2023).

Author contributions. CLB developed the concept of the wind rotor as a sensor, formulated the harmonic-based neural observers in collaboration with MB, and co-supervised the research together with JG. MB implemented the observers, performed all numerical observations, their pre- and post-processing and analysis. CRS conceptually contributed to the pre-processing analysis. PJM and MB processed the raw data
280 from the field measurements. JF performed the aeroservoelastic simulations for the wind speed observer, MB post-processed their results. All authors equally contributed to the interpretation of the results. MB and CLB wrote the manuscript, with contributions by CRS and by JG, PJM, JF, and AW in the description of the test site and the processing of the lidar data. All authors provided important input to this research work through discussions and feedback and by improving the manuscript.

Competing interests. The contact author has declared that none of the authors has any competing interests, except for CLB who is the Editor
285 in Chief of the Wind Energy Science journal.

Financial support. This work is supported in part by the Power Tracker (FKZ: 03EE2036A), Life Odometer (FKZ: 03EE3037B), HighRE (FKZ 03EE2001) and Testfeld BHV (FKZ 0324148) projects, which receive funding from the German Federal Ministry for Economic Affairs and Climate Action (BMWK). This work has also been partially supported by the MERIDIONAL project, which receives funding from the European Union's Horizon Europe Programme under the grant agreement No. 101084216.

290 References

- Bertelè, M., Bottasso, C. L., and Schreiber, J.: Wind inflow observation from load harmonics: initial steps towards a field validation, *Wind Energy Science*, 6, 759–775, <https://doi.org/10.5194/wes-6-759-2021>, 2021.
- Bertelè, M., Meyer, P. J., Sucameli, C., Fricke, J., Wegner, A., Gottschall, J., and Bottasso, C. L.: Figures: The rotor as a sensor — Observing shear and veer from the operational data of a large wind turbine, <https://doi.org/10.5281/zenodo.8335021>, 2023.
- 295 Bishop, C. M.: *Pattern recognition and machine learning*, Springer, New York, 2006.
- Bottasso, C. L. and Riboldi, C. E. D.: Estimation of wind misalignment and vertical shear from blade loads, *Renewable Energy*, 62, 293–302, <https://doi.org/https://doi.org/10.1016/j.renene.2013.07.021>, 2014.
- Bottasso, C. L., Cacciola, S., and Schreiber, J.: Local wind speed estimation, with application to wake impingement detection, *Renewable Energy*, 116, 155–168, <https://EconPapers.repec.org/RePEc:eee:renene:v:116:y:2018:i:pa:p:155-168>, 2018.
- 300 Bromm, M., Vollmer, L., and Kühn, M.: Numerical investigation of wind turbine wake development in directionally sheared inflow, *Wind Energy*, 20, 381–395, <https://doi.org/https://doi.org/10.1002/we.2010>, 2017.
- Burden, F. and Winkler, D.: *Bayesian Regularization of Neural Networks*, pp. 23–42, Humana Press, Totowa, NJ, https://doi.org/10.1007/978-1-60327-101-1_3, 2009.
- Clifton, A., Clive, P., Gottschall, J., Schlipf, D., Simley, E., Simmons, L., Stein, D., Trabucchi, D., Vasiljevic, N., and Würth, I.:
- 305 IEA Wind Task 32 Wind Lidars — Identifying and Mitigating Barriers to the Adoption of Wind Lidars, *Remote Sensing*, 10, 406, <https://doi.org/10.3390/rs10030406>, 2018.
- Coleman, R. P. and Feingold, A. M.: *Theory of self-excited mechanical oscillations of helicopter rotors with hinged blades: Technical Report*, 1958.
- Eggleston, D. M. and Stoddard, F.: *Wind turbine engineering design*, Van Nostrand Reinhold, New York, <https://www.osti.gov/biblio/5719832>, 1987.
- 310 Fleming, P. A., Gebraad, P. M., Lee, S., van Wingerden, J.-W., Johnson, K., Churchfield, M., Michalakes, J., Spalart, P., and Moriarty, P.: Evaluating techniques for redirecting turbine wakes using SOWFA, *Renewable Energy*, 70, 211–218, <https://doi.org/https://doi.org/10.1016/j.renene.2014.02.015>, special issue on aerodynamics of offshore wind energy systems and wakes, 2014.
- 315 Fricke, J., Wiens, M., Requate, N., and Leimeister, M.: Python Framework for Wind Turbines Enabling Test Automation of MoWiT, *Modelica Conferences*, pp. 403–409, <https://doi.org/10.3384/ecp21181403>, 2021.
- Gebraad, P. M. O., Teeuwisse, F. W., van Wingerden, J. W., Fleming, P. A., Ruben, S. D., Marden, J. R., and Pao, L. Y.: Wind plant power optimization through yaw control using a parametric model for wake effects—a CFD simulation study, *Wind Energy*, 19, 95–114, <https://doi.org/https://doi.org/10.1002/we.1822>, 2016.
- 320 Giyanani, A., Sjöholm, M., Rolighed Thorsen, G., Schuhmacher, J., and Gottschall, J.: Wind speed reconstruction from three synchronized short-range WindScanner lidars in a large wind turbine inflow field campaign and the associated uncertainties, *Journal of Physics: Conference Series*, 2265, 022 032, <https://doi.org/10.1088/1742-6596/2265/2/022032>, 2022.
- Gottschall, J., Courtney, M. S., Wagner, R., Jørgensen, H. E., and Antoniou, I.: Lidar profilers in the context of wind energy—a verification procedure for traceable measurements, *Wind Energy*, 15, 147–159, <https://doi.org/10.1002/we.518>, 2012.

- 325 Huhn, M. L. and Gómez-Mejía, A. F.: Aeroelastic model validation with 8 MW field measurements: Influence of constrained turbulence with focus on power performance, *Journal of Physics: Conference Series*, 2265, 032 058, <https://doi.org/10.1088/1742-6596/2265/3/032058>, 2022.
- Hung, L.-Y., Santos, P., and Gottschall, J.: A comprehensive procedure to process scanning lidar data for engineering wake model validation, *Journal of Physics: Conference Series*, 2265, 022 091, <https://doi.org/10.1088/1742-6596/2265/2/022091>, 2022.
- 330 IEC: Wind energy generation systems – Part 50-2: Wind measurement – Application of ground-mounted remote sensing technology, 2022.
- Kim, K.-H., Bertelè, M., and Bottasso, C. L.: Wind inflow observation from load harmonics via neural networks: A simulation and field study, *Renewable Energy*, 204, 300–312, <https://doi.org/https://doi.org/10.1016/j.renene.2022.12.051>, 2023.
- Matlab: Deep Learning Toolbox, <https://www.mathworks.com/help/deeplearning/>, last accessed 20 July 2023, 2023.
- Meyer, P. J. and Gottschall, J.: Evaluation of the “fan scan” based on three combined nacelle lidars for advanced wind field characterisation, *Journal of Physics: Conference Series*, 2265, 022 107, <https://doi.org/10.1088/1742-6596/2265/2/022107>, 2022.
- 335 Meyers, J., Bottasso, C., Dykes, K., Fleming, P., Gebraad, P., Giebel, G., Göçmen, T., and van Wingerden, J.-W.: Wind Farm Flow Control: Prospects and Challenges, *Wind Energy Science*, 7, 2271–2306, <https://doi.org/10.5194/wes-7-2271-2022>, 2022.
- Schreiber, J., Bottasso, C. L., and Bertelè, M.: Field testing of a local wind inflow estimator and wake detector, *Wind Energy Science*, 5, 867–884, <https://doi.org/10.5194/wes-5-867-2020>, 2020.
- 340 Soltani, M. N., Knudsen, T., Svenstrup, M., Wisniewski, R., Brath, P., Ortega, R., and Johnson, K.: Estimation of Rotor Effective Wind Speed: A Comparison, *IEEE Transactions on Control Systems Technology*, 21, 1155–1167, <https://doi.org/10.1109/TCST.2013.2260751>, 2013.
- Vollmer, L., Steinfeld, G., Heinemann, D., and Kühn, M.: Estimating the wake deflection downstream of a wind turbine in different atmospheric stabilities: an LES study, *Wind Energy Science*, 1, 129–141, <https://doi.org/10.5194/wes-1-129-2016>, 2016.
- 345 Wegner, A., Huhn, M. L., Mechler, S., and Thomas, P.: Identification of torsional frequencies of a large rotor blade based on measurement and simulation data, *Journal of Physics: Conference Series*, 2265, 032 021, <https://doi.org/10.1088/1742-6596/2265/3/032021>, 2022.